



Effect of heating surface morphology on the size of bubbles during the subcooled flow boiling of water at low pressure

C. Paz^{*}, M. Conde, J. Porteiro, M. Concheiro

School of Industrial Engineering – University of Vigo, Lagoas-Marcosende, 36310-E, Spain



ARTICLE INFO

Article history:

Received 17 April 2015

Received in revised form 1 June 2015

Accepted 1 June 2015

Available online 14 June 2015

Keywords:

Subcooled flow boiling

Surface morphology

Bubble density

Bubble size

Image processing

ABSTRACT

An experimental investigation on the forced convective subcooled flow boiling of water was carried out using image processing. Three copper test parts of different roughness were tested at different operational conditions established through a design of experiments, covering bulk velocities from 0.1 m/s to 0.9 m/s, bulk temperature from 76.5 °C to 93.5 °C, and operating pressures from 110 kPa to 190 kPa. The boiling process has been maintained on the nucleate regimen varying heat flux from 0.1 MW/m² to 1 MW/m², though image processing was only feasible below 0.65 MW/m². The result of the experimental work is a database of the size distribution of the bubbles at each experimental point and presented as an electronic annex. The results confirmed that bubbles are generally smaller at higher pressure, higher velocities and higher levels of subcooling. The effect of surface morphology proved to be a very strong factor that is normally ignored by correlations and experimental works. Finally, an analysis of the possibility of the interaction of surface morphology with bubble size is presented.

© 2015 Elsevier Ltd. All rights reserved.

1. Introduction

Due to its unquestionable industrial interest, the study of subcooled nucleate flow boiling has received considerable attention over recent decades. Despite the enormous effort made to gain insight into the processes involved, there are still many uncertainties and much contradictory experimental evidence, which make boiling an unresolved issue [1]. Hundreds of studies have tackled the process of boiling at its different scales, employing different fluids, operating conditions, absence of gravity, etc. and with very different methodologies [2–5]. Most of the works devoted to nucleate boiling have served to develop a quite large menu of correlations covering an enormous range of fluids, operational conditions and features of the heating element, so that boiling is manageable at the industrial scale today. Due to their limited range of validation, those correlations need to be carefully selected to produce solid results and can rarely be applied to new situations, geometries, materials, etc. Hence, the study of boiling has never lost interest as new challenges appear every time a new development is made.

To increase the range of applicability, which is the main drawback of the pure empirical correlations, some of the correlations are formulated with a mechanistic basis [6]. Over the years, several

aspects and operational conditions of the boiling phenomenon have been noted to be essential, and therefore, some correlations are based on the individual characterisation of those key subprocesses and dependences [4] [7–9]. In the case of subcooled nucleate flow boiling, it has been noted that the whole process can be considered to be the conjunction of liquid fluid forced convection, transient conduction under and around the emerging bubbles, and microlayer evaporation at the interface of the bubble and the heating surface. Consequently, most of the processes are linked to the nucleation, growth, and departure of the bubbles, and therefore, the precise determination of their density, frequency, and size are the core of most mechanistic-based correlations used currently.

Bubble behaviour in subcooled flow boiling has been investigated by several researchers, starting in 1951 with the work by Gunther [10], who was the first to employ high-speed photography to quantify the size, lifetime, and growth of bubbles under different operational conditions. Tolubinsky and Kostanchuk [11] studied the flow boiling of water on a horizontal stainless steel plate and found a strong dependence between bubble size and pressure, especially at pressures close to atmospheric. Abdelmeseih [12] used high-speed photography to study the effect of flow velocity on bubble dynamics at artificial nucleation sites. They found that the increase in liquid velocity resulted in a decrease in bubble size, which was contradictory to the conclusions of Gunther. Bibeau and Salcudean [13] reported discrepancies between the experimental results and the theoretical prediction of bubbles sizes at low

^{*} Corresponding author.

E-mail address: cpaz@uvigo.es (C. Paz).

Nomenclature

D_b	bubble diameter [m]	T_{sat}	saturation temperature [K]
k	thermal conductivity [$\text{W m}^{-1} \text{K}^{-1}$]	T_{wall}	wall temperature [K]
M_{r1}	peak material component	ΔT	$= T_{12} - T_{22}$
M_{r2}	valley material component	ΔT_{sub}	subcooling [K]
p	pressure [Pa]	v	velocity
q''	heat flux [W m^{-2}]	Δx_{12}	distance between thermocouples [m]
R_a	arithmetic mean roughness height [μm]	Δx_w	distance from thermocouple 11 to the wall [m]
R_{pk}	reduced peak height [μm]		
R_q	root-mean-square roughness [μm]		
R_t	maximum peak-to-valley height [μm]		
R_{vk}	reduced valley depth [μm]		
R_z	ten-point height [μm]		
S_a	arithmetic mean surface height [μm]		
S_q	root-mean-square surface height [μm]		
S_z	maximum surface height [μm]		
T_{12}	thermocouple 12 temperature [K]		
T_{22}	thermocouple 22 temperature [K]		
T_b	bulk temperature [K]		

Abbreviations:

FDB	fully developed boiling
HTC	heat transfer coefficient
NVG	net vapour generation
ROI	region of interest

Greek:

ε	error
---------------	-------

pressure. They found that bubbles reach a higher size during their growth and that their departure started with a smaller diameter, which implied that condensation had started before departure. This fact was later reported by Zeitoun and Shoukri [14].

If we extend the discussion to the whole range of boiling, from the very beginning, the condition and morphology of the heating element was recognized to be a factor of boiling heat transfer. In 1936, Jakob [15] reported that the morphology, corrosion, and oxidation of the heating element produced a drift in the boiling curve towards higher wall temperatures. In fact, the earliest correlation for pool boiling, proposed by Rohsenow [16] employed a proportionality constant that was dependent on the heater-fluid material combination. At that moment, no explicit influence of roughness was noted, but posterior works observed such influence [17,18].

Decades after Jakob's work, several studies revealed that bubbles were generally emanated from cavities and other singularities, and theories were formulated to establish the conditions that make a cavity a valid candidate for the nucleation of a new bubble. Corty and Foust [17] were probably the first to study the effect of surface roughness by employing different levels of polishing of copper and nickel surfaces. Bankoff [19] showed that only unwetted cavities can develop a bubble and that the shape of the cavity was critical in the trapping of vapour. He formulated a geometric criterion that established that the angle of the cavity had to be small enough in comparison with the liquid-surface contact angle to avoid the re-flooding of the cavity. Griffith and Wallis [20] found a relationship between the size of the cavity and the superheating required for nucleation. Berenson [21] studied the effect of surface roughness on the boiling curve and concluded that surface roughness should be included as an important parameter but that R.M.S. roughness is not suitable for that purpose. On the other hand, Bergles and Rohsenow [22] initially stated that commercial surfaces have such a vast variety of cavities that boiling should be surface condition independent, though this was later discussed by Mikic and Rohsenow [23].

In 1962, Hsu developed a criterion to link bubble nucleation and cavity size [24]. According to Hsu, the requisite for the nucleation site to become active is for the surrounding temperature of the bubble, placed as a half sphere on the edge of the cavity mouth, to be equal to or exceed the saturation temperature that corresponds to the pressure inside the bubble, which is estimated by balancing pressure and surface tension forces. This criterion, extensively applied and revised during the last 50 years,

establishes the range of cavity sizes that may become active. Hence, bubble nucleation is directly related to surface morphology; however, if cavities are not conical, Hsu's criterion is difficult to apply. It has been reported that grooves, which are commonly the type of roughness observed in industrial applications, are ineffective vapour traps unless they are very steep or the surface is poorly wetted by the fluid, and therefore conduct to a misleading relationship between roughness and boiling enhancement. On the other hand, a 'rough' surface in terms of boiling for a regular fluid can be 'smooth' for a fluid with a high wettability [25]. It has also been reported that the presence of cavities on the surface is not required for heterogeneous nucleation [1]. Hence, the relationship between active cavities and the surface micro-structure is one of the key unsolved issues in the prediction of nucleate boiling heat transfer [26].

Additionally, single vertical parameters employed to quantify roughness, such as R_a , R_p or R_q , cannot characterize the shape and size of cavities, hence their impact on boiling. This has led to the development of other 2D or 3D parameters based on the cone angle or cavity mouth size [6], [27]. Recently, due to the clear influence of the bubble scales on the interaction of surface morphology and boiling, fractal analysis has been used with some promising results [28].

It has been noted that re-flooding of the cavities is a key in their reactivation, which is influenced by the wetting contact angle (WCA). It is generally observed that contact angle decreases with roughness [6] and changes with the nature of the coating [29] and that the contact angle made by the liquid-vapour interface at the base of the bubble with the wall varies during bubble growth and departure. Additionally, physical changes in the micro-structure of the heating surface due to erosion, chemical reaction, the filling of the pores and cavities with impurities, corrosion, oxidation, etc. have been reported to occur during boiling and produce a general decrease in HTC [1], [30,31]. These processes, generally lumped together as 'aging', tend to improve the wettability of the surface, leading to an unsuccessful trapping of vapour in the cavities and hence to a reduction in the number of active sites based on the Bankoff criteria. In fact, Wang and Dhir [32] found that the number density of active sites for a given cavity diameter decreased by a factor of 25 when the contact angle was reduced from 90° to 18° by controlling the degree of oxidation of their copper surfaces in water. In addition, the contact angle is affected by the drag forced exerted by the flow, hence, a precise measurement

of it and its influence on a bubble's growth and departure is still an open issue [33–35].

However, the effect of the heater on bubble dynamics cannot be limited to its morphology and contact angle. Kutateladze proposed that the effect of the surface on boiling could be expressed in the form of a ratio of their thermal effusivities [25], which from a mechanistic point of view, can be seen as the thermal response of the surface-liquid interface when the fluid replaces the volume abandoned by the departing bubble. Actually, the thermal response of the surface can produce a broader effect. For high conductivity surfaces, the overheating around an active site will spread easily and the condition for bubble formation will not be fulfilled, leading to the deactivation of the surrounding areas. On the contrary, a low conductivity surface can sustain several active sites in the same region, leading to a better use of their potential nucleation sites [36].

Hatton and Hall [37] considered all of the forces during the growth of a bubble and postulated that bubble departure size is mainly determined by the balance between buoyancy and dynamic lateral forces. Unal [38] formulated a model based on a spherical bubble growing on a very thin, partially dried liquid film formed between the bubble and the wall. The bubble was assumed to receive heat by evaporation from the thin film and to dissipate heat by condensation in its upper half. It was determined that bubbles leave the wall once they reach their maximum diameter. Klausner et al. [39] performed a detailed analysis on the forces acting on a bubble to predict the mean departure diameter. The model predicted a strong reduction of bubble departure diameter as the velocity of the flow increased and corroborated that the inertia of the surrounding liquid being displaced during bubble growth was a main force of adhesion. Kandlikar [40] formulated a similar model based on the longitudinal and vertical forces acting on a bubble and found that the departure diameter was smaller and that the upstream and downstream contact angles went through maximum and minimum values, respectively, as the flow velocity was increased. However, despite the extensive work conducted on the modelling of bubble dynamics and after several decades of development, the scales involved and the interrelation between temperature and the velocity fields between the bubbles, the surrounding liquid and the surface and their effect on bubbles' departure diameter are still unresolved [34]. Very recently, Colombo and Fairweather [41] presented a revision of the model proposed by Klausner and attained a good agreement between their model in the prediction of bubble departure diameter and the available experimental databases.

The work presented in this paper describes the experimental investigation of the effect of surface morphology on the size distribution of the bubbles emitted from horizontal flat surfaces of copper under subcooled flow boiling of water at low pressure, understanding by low pressure those common in subcooled boiling literature (i.e. 100–500 kPa). An optical interferometer has been used to scan the micromorphology of the surfaces employed, and high-speed recording and an ad-hoc image recognition algorithm were used to measure the size of the bubbles. The goal of this work is to obtain bubble size data under different operational conditions and to discuss the potential influence of the shape and microstructure of the heating element on the size of the bubbles. All the experimental acquired data, that comprised more than 1.15 million bubbles analysed, are gathered in the attached electronic files.

2. Experimental setup

The test bench (Fig. 1) designed to carry out the experiments consists in two main parts: the test section (Fig. 2) and the piping and other auxiliary devices, which control the conditions of the

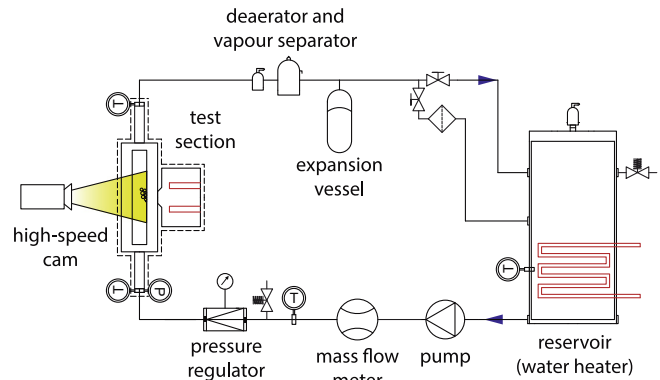


Fig. 1. Test bench sketch.

tests in terms of pressure, velocity and temperature. Further information regarding the experimental facility can be found in [42]. Due to the fact that one of the goals of this work is the measure of the bubble's diameter, it was necessary to attach the recording system to the original bench. It comprises a high-speed camera with an operating frame ratio up to 10,000 fps and two LED lamps, with 7700 lm each and a total power of 84 W. At the standard recording speed of 8000 fps, the sensor resolution is 400×170 pixel, and with the 50 mm focal length lens used, the recorded dimensions were 23.5×10 mm.

2.1. Test section

The test section consists in a rectangular channel of 25×20 mm with a total length of 1200 mm, made of stainless steel. The hot zone was placed at the bottom of the central section, whereas the lateral and the upper walls were designed as polycarbonate windows for lighting and filming purposes.

The three copper test parts employed in this work were made from the same block of electrolytic copper, but different surface finishing methods were applied to their 'wet face'. The smoother surface (coded PLs) was hand finished with fine sanding (FS) to attain a R_a below $0.2 \mu\text{m}$, the intermediate surface finish (coded PLm) was formed by Electrical Discharge Machining (EDM) followed by fine sanding (R_a approximately $1.7 \mu\text{m}$) whereas the rough surface (coded PLr) was made by only EDM (R_a near $8 \mu\text{m}$). The common morphological parameters for the three parts are shown in Table 1. These parameters have been measured with a noncontact optical profiler (NT1100 of WYKO-Veeco) after performing microscopic analyses of areas up to 10×5 mm for each of the heating surfaces. Due to the range in vertical height to measure, speed and required resolution and area to cover, an optical profiler was selected as classic contact profilers or electron microscopy did not offer the same performance in terms of 3D resolution and area covered. Fig. 3 shows a 3D characterization of one subarea of each surface tested, PLs, PLm and PLr. At the bottom of the image, random profiles were plotted for each of the surfaces. As shown, PLs could be considered as a technically smooth surface, PLm is characterized by grooves and holes and PLr has grooves, holes, peaks and crests. The aim here is to describe the macro morphology of the test parts even though additional topography information about the test surfaces, before and after the test, can be found in a previous work [42].

2.2. Experimental methodology

A central composite design of experiments (DOE) was made to analyse the operating conditions of the fluid, employing five

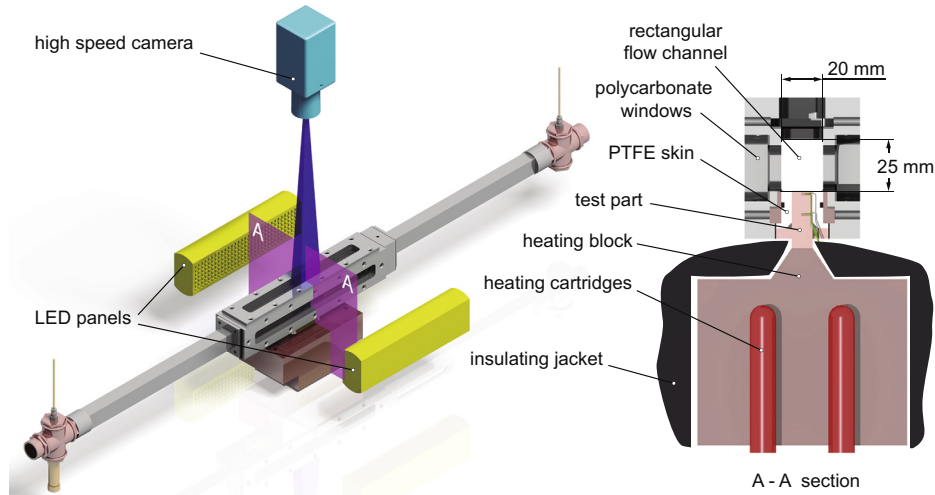


Fig. 2. Test section. Left: recording system. Right: cross section of the target area.

Table 1
Test parts roughness parameters.

Designation	Material	Surface finish	R_a [μm]	R_q [μm]	R_t [μm]	R_z [μm]	S_a [μm]	S_q [μm]	S_z [μm]	M_{r1} [%]	R_{pk} [μm]	M_{r2} [%]	R_{vk} [μm]
PLs	Copper	FS	0.17	0.24	3.51	2.82	0.18	0.24	2.49	9.41	0.22	88.4	0.31
PLm	Copper	EDM + FS	1.67	2.48	26.3	21.6	1.63	2.48	17.8	5.55	0.35	76.8	6.18
PLr	Copper	EDM	7.88	9.73	59.9	57.6	7.88	9.72	47.6	9.79	8.96	91.2	7.61

temperature levels, pressure and velocity. The resulting test matrix and the code-number of every test are graphically shown in Fig. 4 and the operational conditions for the 15 resulting experimental conditions are listed in Table 2.

Once the 15 experimental conditions were determined, footages of the phenomena at 10 discrete values of heating flux ranging from 200 kW/m^2 to 650 kW/m^2 , were recorded. On average, these 150 short films contain almost 115,000 frames per analysed part, that is, about 340,000 for the three parts. As a result, more than 1,150,000 bubbles were identified, tracked, post-processed and presented as an electronic annex of the paper.

The wall heat flux is calculated by reading the values of the thermocouples (k-type, class-2 tolerance, 0.5 mm diameter and 0.03 s response time) embedded in the test part and arranged as shown in Fig. 5. Although three pairs have been mounted, only the middle values T12 and T22 (i.e. those located in the recorded area) are used for heat flux calculation assuming Fourier's law. The left and right values are used to check a minimum required homogeneity in the part's field of temperatures. Once the heat flux is known a value for the wall temperature is estimated by extrapolation.

The bulk velocity is calculated averaging the mass flow rate, which is measured with an ultrasonic flow meter and a declared tolerance of $\pm 0.5\%$, with the total cross section. To estimate the subcooling a Gems Psibar® CVD 2200 series pressure transducer located at the inlet of the test zone together with two PT100 – A class temperature sensors at the inlet and the outlet have been mounted. The bulk temperature is assumed to be equal to the inlet value. The relative location of these and other elements can be consulted in Fig. 1.

To reduce the impact of the aging effect on the results, several cycles of control tests were carried out during a minimum of 50 boiling-hours until the repeatability of the results was good enough. An example of the aging process for the part PLs is shown in Fig. 6. The selected global criteria to assume the part completely aged was a R.M.S. percent difference between two adjacent curves

below 5%. Once the surface is aged, the test protocol started. Additional measures were taken to avoid any influence from a particular test on the subsequent ones. For example, deionized water of the test loop was completely renewed after each test part assembly and after that, new water was heated and the entire system was degassed by boiling during several hours.

2.2.1. Uncertainty analysis

In order to quantify the accuracy of the main variables measured in this work a study of the uncertainties was performed, based in the manufacturing tolerances, thermocouples and pressure sensors accuracy and the precision of the functions modelling the thermodynamic properties. The temperature measuring arrangement had to be calibrated to rise the global accuracy and to determine the offset values for each of the thermocouples. Also the machine vision system was calibrated making several measuring tests using a metal sheet with graduated marks and little steel balls after each batch of experiments. The maximum estimated uncertainties for the main variables, measured or derived, are shown in Table 3.

Derived uncertainties have been calculated using the common theory of errors. For instance, the uncertainty when estimating the heat flux has been calculated according to Eq. (1)

$$\varepsilon_{q_w} = \left[\left(\frac{\partial q_w}{\partial k} \right)^2 \varepsilon_k^2 + \left(\frac{\partial q_w}{\partial (\Delta T)} \right)^2 \varepsilon_{\Delta T}^2 + \left(\frac{\partial q_w}{\partial (\Delta x_{12})} \right)^2 \varepsilon_{\Delta x_{12}}^2 \right]^{0.5} \\ = \left[\left(\frac{-\Delta T}{\Delta x_{12}} \right)^2 \varepsilon_k^2 + \left(\frac{-k}{\Delta x_{12}} \right)^2 \varepsilon_{\Delta T}^2 + \left(\frac{k \cdot \Delta T}{(\Delta x)^2} \right)^2 \varepsilon_{\Delta x_{12}}^2 \right]^{0.5} \quad (1)$$

where

$$\varepsilon_{\Delta T} = \varepsilon_{(T_{12}-T_{22})} = \left[\left(\frac{\partial (\Delta T)}{\partial T_{12}} \right)^2 (\varepsilon_{T_{12}})^2 + \left(\frac{\partial (\Delta T)}{\partial T_{22}} \right)^2 (\varepsilon_{T_{22}})^2 \right]^{0.5} = \sqrt{2} \cdot \varepsilon_{T_{12}} \quad (2)$$

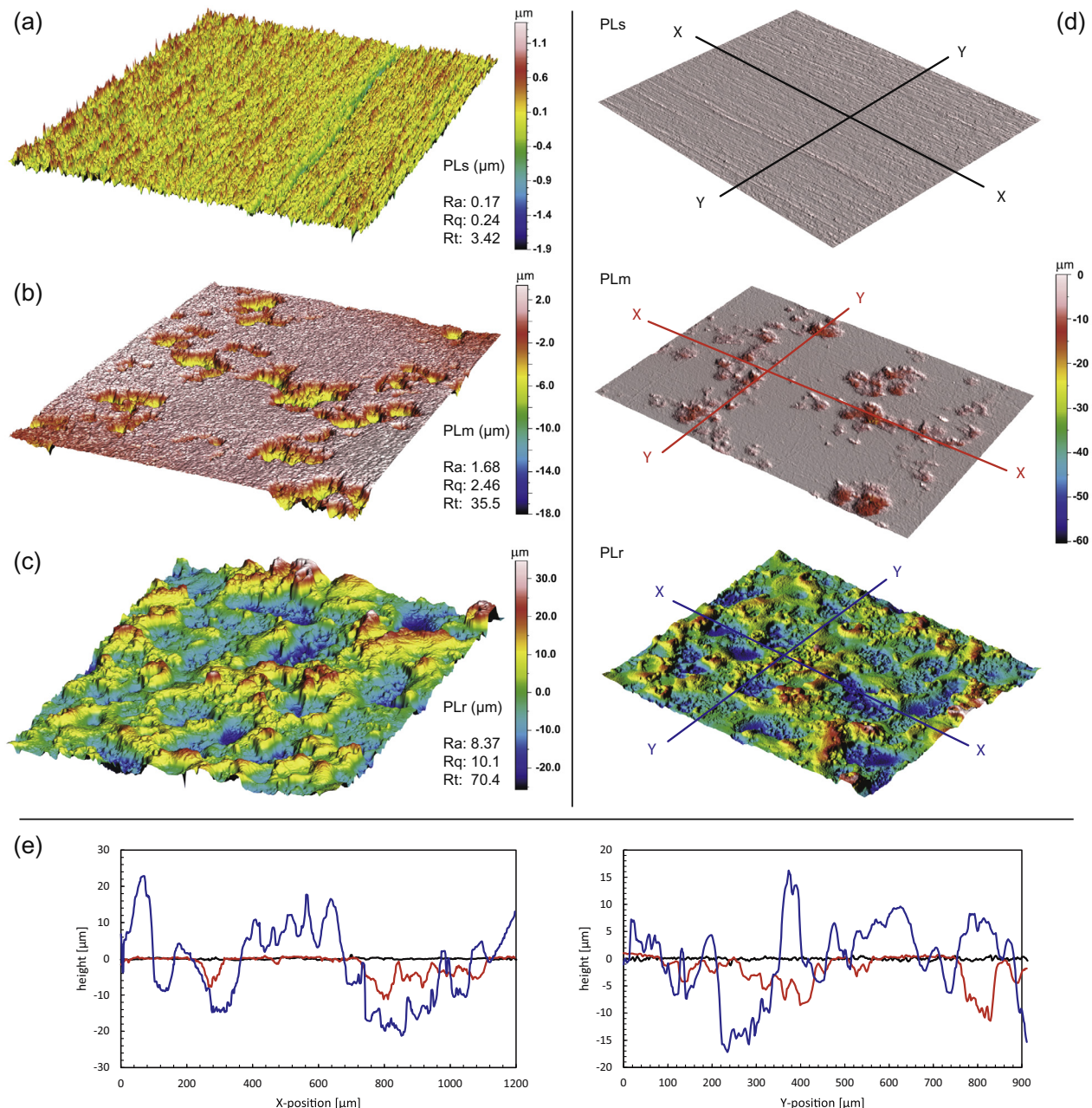


Fig. 3. Morphology of the test parts employed. Left: PLs (a), PLm (b) and PLr (c); right: same colour map. Bottom: random X and Y cross section profiles for PLs (black), PLm (red) and PLr (blue). Cutting planes are shown in the images of the right. (For interpretation of the references to colour in this figure legend, the reader is referred to the web version of this article.)

The maximum estimated uncertainty on the wall heat flux is about $\pm 7.5\%$ whereas for the wall superheating is less than $\pm 2.5^\circ\text{C}$, both measured at the final FDB stretch. An example of the uncertainty when calculating the wall heat flux is shown in Fig. 7 for the boiling curve of the part PLs and test point No. 8.

2.3. Image processing

A general overview of the bubble recognition algorithm is shown in Fig. 8. General speaking, it comprises three main steps: frame acquisition (pre-processing), bubble detection (processing) and generated data post-processing. The pre-process required is very simple, consisting in the extraction of frames from the video footage. The subsequent stages are explained in the following subsections.

2.3.1. Bubble detection

For bubble detection, an ad hoc image processing software based on the .NET™ libraries of the machine vision software Halcon© was developed. After the first step of defining the region of interest (ROI), each frame was examined for the presence of bubbles. The identification of a bubble is based on an illumination effect consisting in two bright areas produced on the lateral of the bubbles as they are illuminated from both sides. To identify these areas the main operation is to perform a dynamic threshold to make the segmentation independent of the global level of illumination (Fig. 9-left). This operation required a background image to compare with and which usually consisted in the same image after applying a smoothing filter. The filter employed was the mean image filter, which performs the convolution of the original

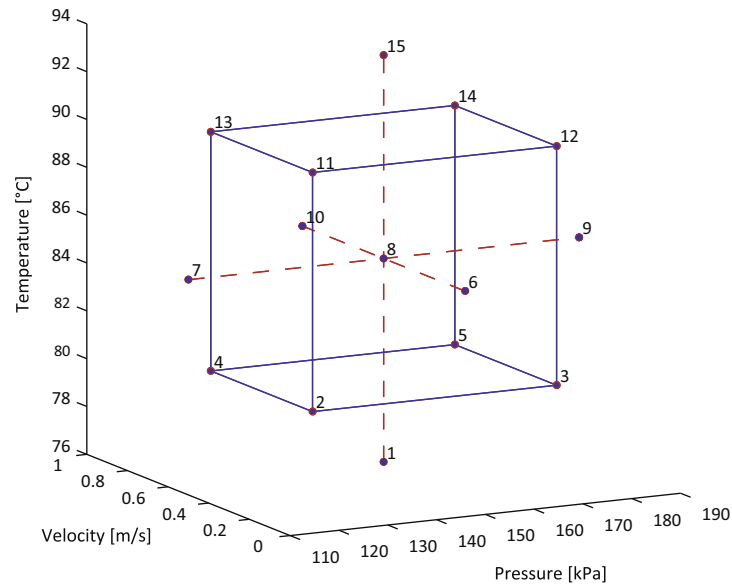


Fig. 4. Test matrix.

Table 2
Experimental points.

Designation	Bulk temp. [°C]	Pressure [kPa]	ΔT_{sub} [°C]	Bulk velocity [m/s]	G [kg/m ² /s]
1	76.5	150	34.8	0.50	487.0
2	80.0	125	26.0	0.75	728.9
3	80.0	175	36.0	0.75	728.9
4	80.0	125	26.0	0.25	243.0
5	80.0	175	36.0	0.25	243.0
6	85.0	150	26.3	0.90	871.8
7	85.0	110	17.3	0.50	484.3
8	85.0	150	26.3	0.50	484.3
9	85.0	190	33.6	0.50	484.3
10	85.0	150	26.3	0.10	96.9
11	90.0	125	16.0	0.75	724.0
12	90.0	175	26.0	0.75	724.0
13	90.0	125	16.0	0.25	241.3
14	90.0	175	26.0	0.25	241.3
15	93.5	150	17.8	0.50	481.5

image, pixel by pixel, using the mean grey value that exists in the predefined mask size given as input.

Once all the bright pixels have been detected they are grouped to identify the possible vapour bubbles that are present in the current frame. To make this “pattern seeking” an algorithm depending on shiny areas distance, relative orientation and brightness between them, has been implemented. The sequential steps of bubble identification are illustrated in Fig. 9 (note that brightness and contrast of 1, 2, A and B images have been manually adjusted for visualization purposes). When all the selected frames have been processed (i.e. all the bubbles have been identified) an ASCII file is generated reporting centre coordinates, diameter and frame for each bubble $[X \ Y \ D \ f]$.

2.3.2. Data post-processing

The ASCII file generated in the previous step is post-processed employing VBA® and Matlab® to identify the path of each bubble over the frame sequence, as well as their size evolution. The first post-processing operation is to refuse all the $[X, Y]$ pairs laying in the ROI boundary, so a discarding fringe is taken into account. The width of this exclusion zone is calculated as a function of the maximum diameters detected in the current frame. After this, a

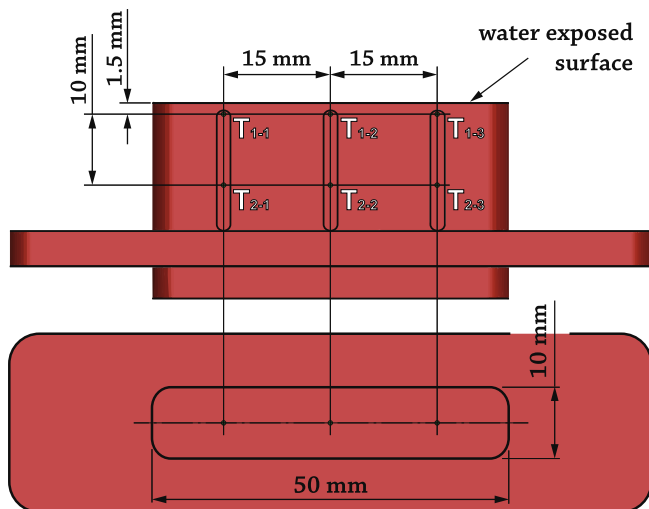


Fig. 5. Test part. Functional dimensions and location of the embedded thermocouples.

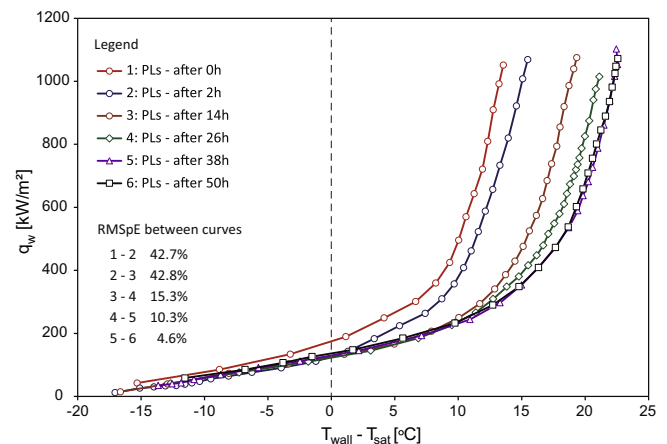
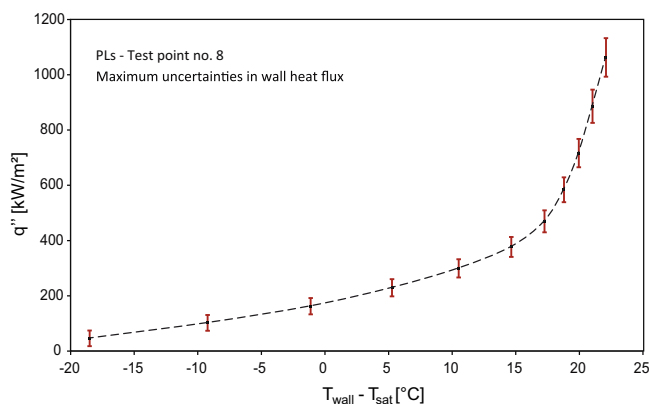


Fig. 6. Aging process for PLs and similarity between adjacent curves.

Table 3
Uncertainties.

Variable	Assumed tolerances	Error@FDB (onset)	Error@FDB (final stretch)
T_{12}, T_{22}	± 0.85 K	–	–
T_b	± 0.35 K	–	–
k	± 0.204 W m ⁻¹ K ⁻¹	–	–
ΔT	± 1.20 K	–	–
v_b	± 4.6 mm s ⁻¹	–	–
Δx_{12}	± 0.6 mm	–	–
Δx_w	± 0.35 mm	–	–
p	± 3000 Pa	–	–
D_b	± 0.029 mm	–	–
T_{sat}	± 1.21 K	–	–
T_w	–	± 0.82 K	± 2.16 K
$T_w - T_{sat}$	–	± 1.45 K	± 2.47 K
q''	–	± 51.8 kW	± 80.2 kW ($\pm 7.4\%$)

**Fig. 7.** Maximum calculated uncertainties for the smoothest surface and the test point No. 8 assuming a known value for the wall superheating.

minimum size filter for the diameter value is needed to avoid considering too small residual vapour fractions, fouling particles and so on, as real bubbles. Although this minimum size is a user defined parameter, it was set to 3 pixel after human-eye validations, which means that 0.177 mm was the minimum diameter recognized with the system employed in this work.

The next stage is the bubble tracking process and the nucleation site identification. It is clear that not all the pairs in the frame

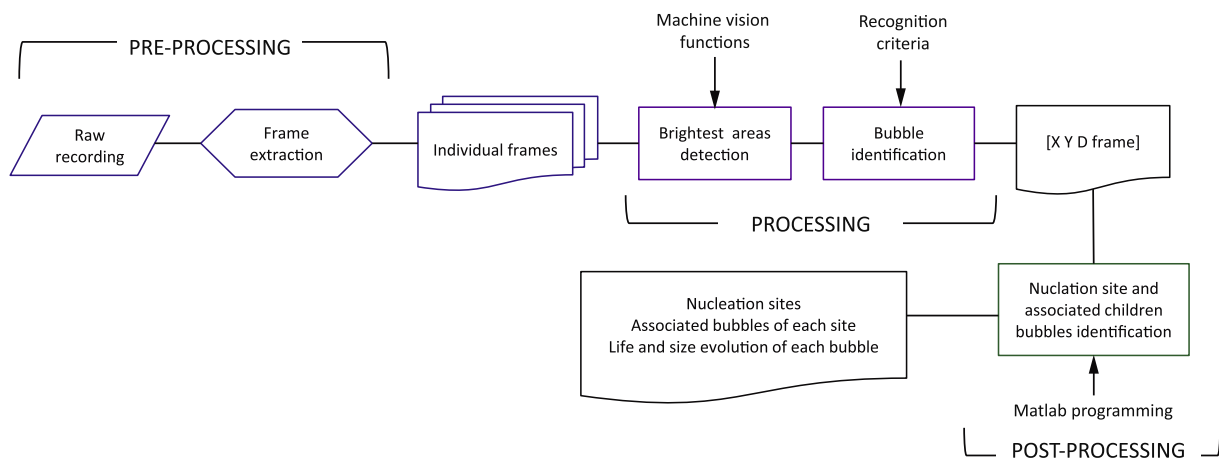
under analysis mean a nucleation site, so to decide if a pair is part of a previously detected bubble or represents a new nucleation site, it is necessary to scan the previous frame to check for the existence of the bubble. Fig. 10 shows graphically the matrix to be processed. Here the pair $[X_1, Y_6]$ at frame n represents a nucleation site, with a start-up diameter $D_{2,n}$ nevertheless the pair $[X_3, Y_3]$ at frame n does not stand for a new site as a previous bubble exists in $[X_4, Y_1]$ at frame $n - 1$. To ensure if this last pair represents a new site a new seeking process must be performed at frame $n - 2$. The past and future seeking area, grey shaded in the image for bubble $[X_3, Y_3, D_{2,n}]$, is a required user input in terms of a pixel gap in X and Y . Doing this recursively until all the bubbles are identified as new sites or simply the evolution of an old one, all the paths and diameter for all the bubbles are identified so that the life-diameter evolution as well as the nucleation site density in each of the frames can be established. Moreover, at the end, the bubble life curve is known for each bubble emerging at a nucleation site, so, the nucleation frequency for each site can be calculated too. The life cycle and the associated life-diameter diagram for a random bubble at a particular nucleation site is showed in Fig. 11.

3. Results

3.1. Bubble density above the heater

Bubble density was defined averaging the total number of observable bubbles in every frame inside the region of interest (ROI) analysed. This include both the sliding bubbles as well as the short-life ones. The evolution of bubble density in relation to heat flux is shown in Fig. 12. As shown, bubble density increases with an increase in the heat flux. It can also be observed that bubble density increases as the velocity of the fluid is reduced. Both are in agreement with previous works [43]. It can be observed that although the aforementioned tendencies seem to be quite consistent, some local disruption of these tendencies can be observed. This has been related by other authors to particle coalescence [44], especially at high heat fluxes and low bulk velocities. As a consequence and due to the difficulties found when identifying bubble diameters practically above 0.6–0.65 kW/m², most of the work was developed under high subcooled conditions that is, hardly overtaking the NVG point.

Regarding surface finish, it seems to have a strong effect on bubble density as the number of bubbles at the same heat flux and same bulk velocity is much higher on the smooth surface than

**Fig. 8.** Bubble recognition algorithm.

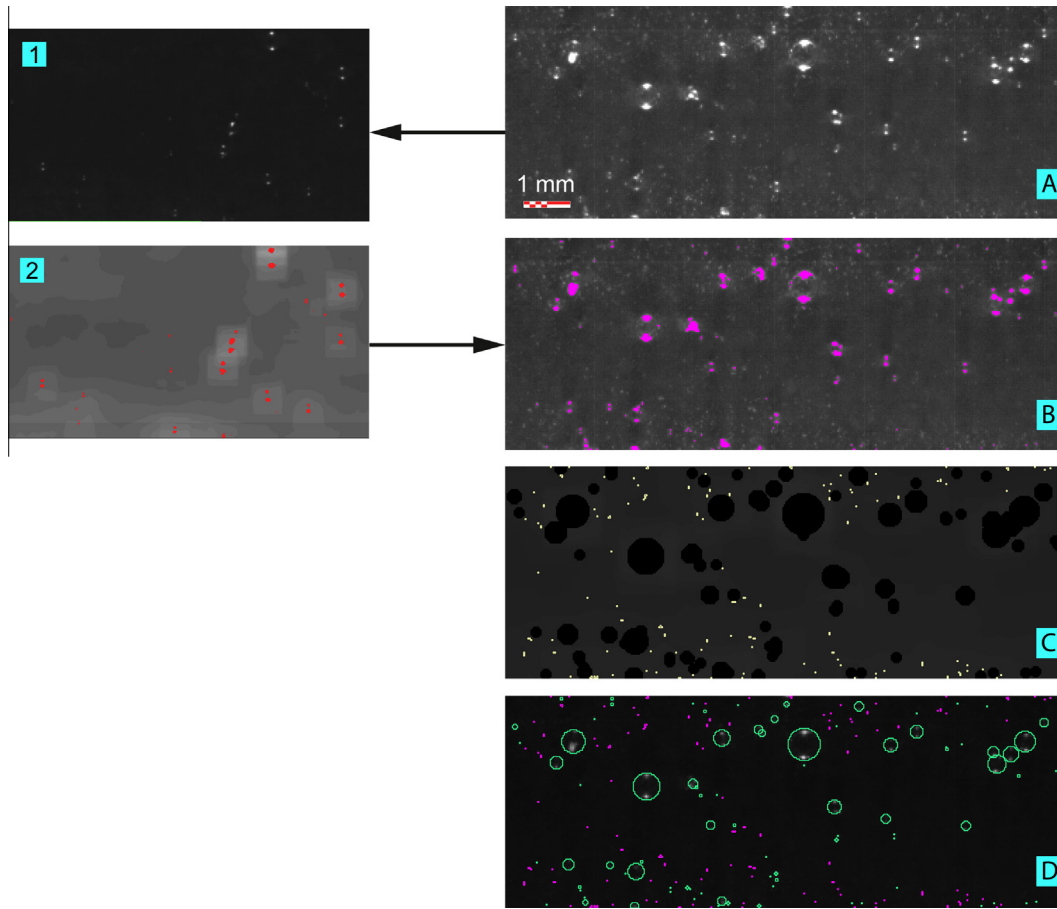


Fig. 9. Left: Original image (1) and segmented image after applying the mean image filter (2). Right: Original image (A), brightest areas (B), residual vapour (C) and final result with identified bubbles in green and residual vapour in magenta (D). (For interpretation of the references to colour in this figure legend, the reader is referred to the web version of this article.)

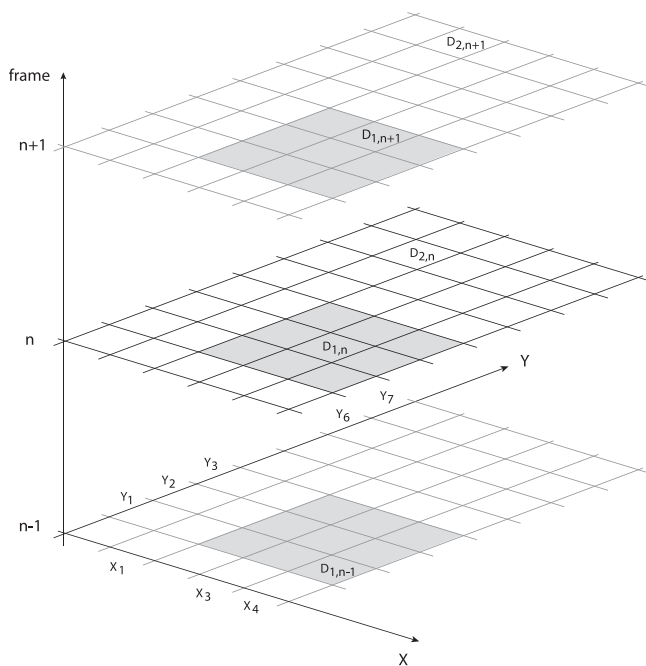


Fig. 10. Multidimensional array $[X Y D f]$ generated in the processing stage.

on the medium and rough finished surfaces. For instance, at 500 kW/m^2 and bulk velocity of 0.1 m/s , their density is 50 bubbles/cm^2 for PLs, 30 bubbles/cm^2 for PLm, and below 20 bubbles/cm^2 in the case of PLr. As surface morphology affects several aspects involved in the heat exchange process (from convection to several mechanisms at the bubble scale) the effect of roughness on bubble density will be discussed later.

3.2. Size distribution

Bubbles in every frame were recognized, interpolated to the morphologically closest sphere, counted, tracked, and aggregated in size ranges based on their maximum diameter. The number of bubbles in each family was later averaged over the timeframe of the experiment. As the complete collection of results will exceed the allowed extension for this manuscript, only a handpicked selection of the data generated will be shown. As aforementioned, the electronic annex contains all the identified bubbles ready for consulting and data mining.

For all of the nucleate sites recognized along the consecutive frames of the entire film, the maximum diameter of the bubbles formed in each of the sites was measured. Subsequently, the statistical mean for the values associated with every site was calculated and the resulting sample, comprising the means of the maximum diameters of each site, was plotted as a histogram. The histograms representing the distribution for the smoothest surface (PLs) at the central point of the hypercube of experiments ($T_b = 85^\circ \text{C}$,

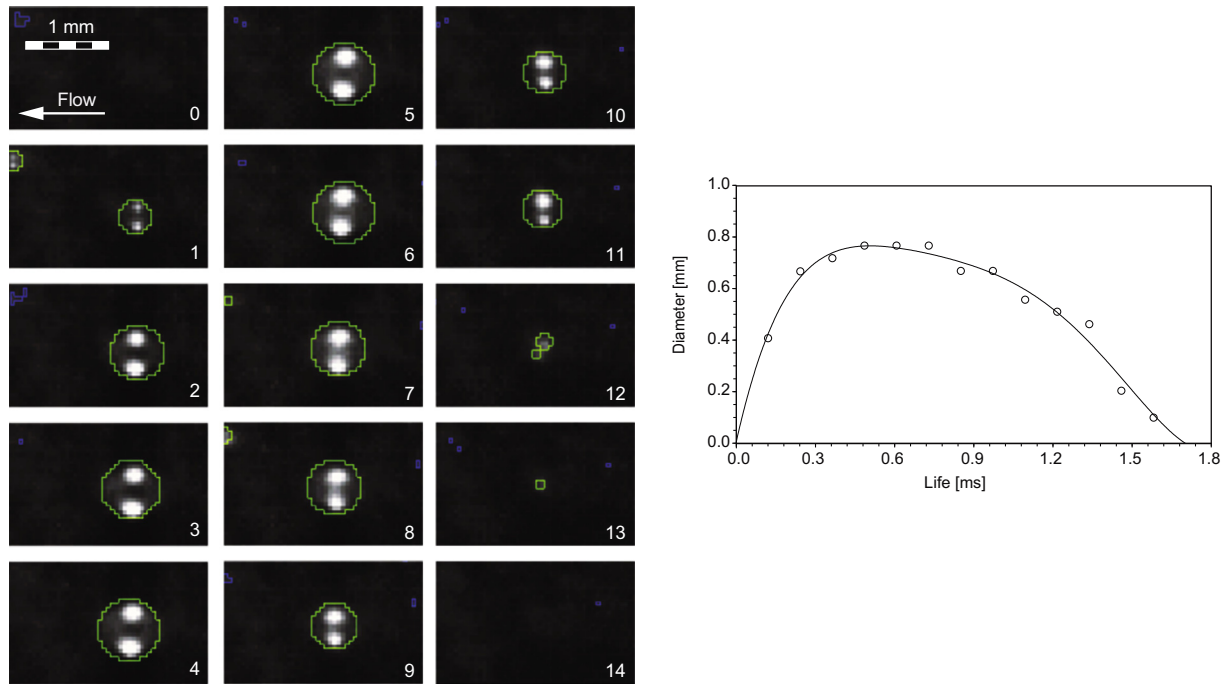


Fig. 11. Example of bubble diameter tracking during its whole life. Left: frame-by-frame detection. Right: resulting diameter vs life diagram.

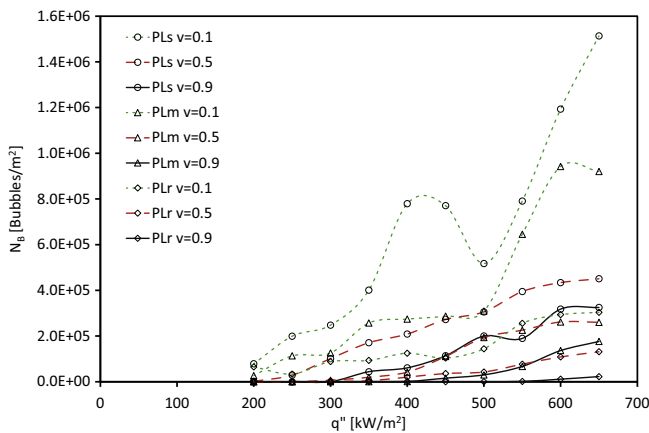


Fig. 12. Bubble density ($T_b = 85^\circ\text{C}$, $\Delta T_{\text{sub}} = 26.3^\circ\text{C}$, $p = 150\text{ kPa}$, $v = 0.1\text{--}0.9\text{ m/s}$).

$\Delta T_{\text{sub}} = 26.3^\circ\text{C}$, $p = 150\text{ kPa}$, $v = 0.50\text{ m/s}$ and heat fluxes 500, 550, 600 and 650 kW/m^2 are shown in Fig. 13.

The bubbles were distributed into several size families in $50\text{ }\mu\text{m}$ increments from $150\text{ }\mu\text{m}$ to higher than $1000\text{ }\mu\text{m}$ (1 mm). The information in the first column of each graph represents the percentage of bubbles with an interpolated spherical diameter below $150\text{ }\mu\text{m}$, and the last column represents the percentage of bubbles higher than 1 mm in diameter. In addition, the best-fit Weibull distribution has been depicted with its statistical data shown in the legend of each graph. It is important to highlight that the number of bubbles included in the tiny and large families were generally below 5% meaning that 95% of the bubbles were correctly measured and categorized. The enormous spread of diameters measured has been extensively reported by previous works and suggests that, in the end, bubble departure has a stochastic nature. The size variability at the moment of depart likely has its origin in the randomness of turbulence fluctuations with length and time

scales in the same range of bubbles cycle [39]; thus, each bubble nucleate grows and departs affected by the instantaneous flow and temperature fields rather than the time-average ones.

3.3. Effect of roughness on bubble size distribution

The results showed a clear difference between the three surfaces tested. To summarize the effect, four sets of curves for each surface finish are shown in Fig. 14. As shown, PLr shows a clear tendency towards smaller bubbles (with a typical diameter of $280\text{ }\mu\text{m}$), with no observed bubbles larger than $600\text{ }\mu\text{m}$, whereas PLm has a typical diameter of $330\text{ }\mu\text{m}$ and a maximum observed size of $700\text{ }\mu\text{m}$. The smoothest surface (PLs) shows a typical diameter of $350\text{ }\mu\text{m}$ and a maximum observed size during these tests of $800\text{ }\mu\text{m}$.

The shape of the distributions also indicates that bubbles generated by the rougher surfaces have a narrower range of diameters than those generated by the smooth one. In addition, the number of tiny bubbles generated seems to be dependent upon surface morphology as PLs generates less than 5% of its bubbles smaller than $150\text{ }\mu\text{m}$, PLm is closer to 7% and PLr reaches 9%.

The impact of roughness on bubble size is in agreement with the findings previous work and has been related to the number pores, [45], their size, [27] and also the modification of the WCA [31].

3.4. Subcooling

The effect of subcooled fluid on the bubble diameter was studied by comparing test points 1, 8 and 15. In Fig. 15 the data for the three surfaces at a heat flux of 600 kW/m^2 are represented. The results show that in the case of PLs, if the level of subcooling decreases, the diameter of bubbles increases. This effect is not detected in the case of PLm and PLr, which will be discussed later in the text.

The influence of subcooling on bubble size is in agreement with most previous experimental data [1,43] and has been attributed to a modification of the temperature field of the surrounding liquid

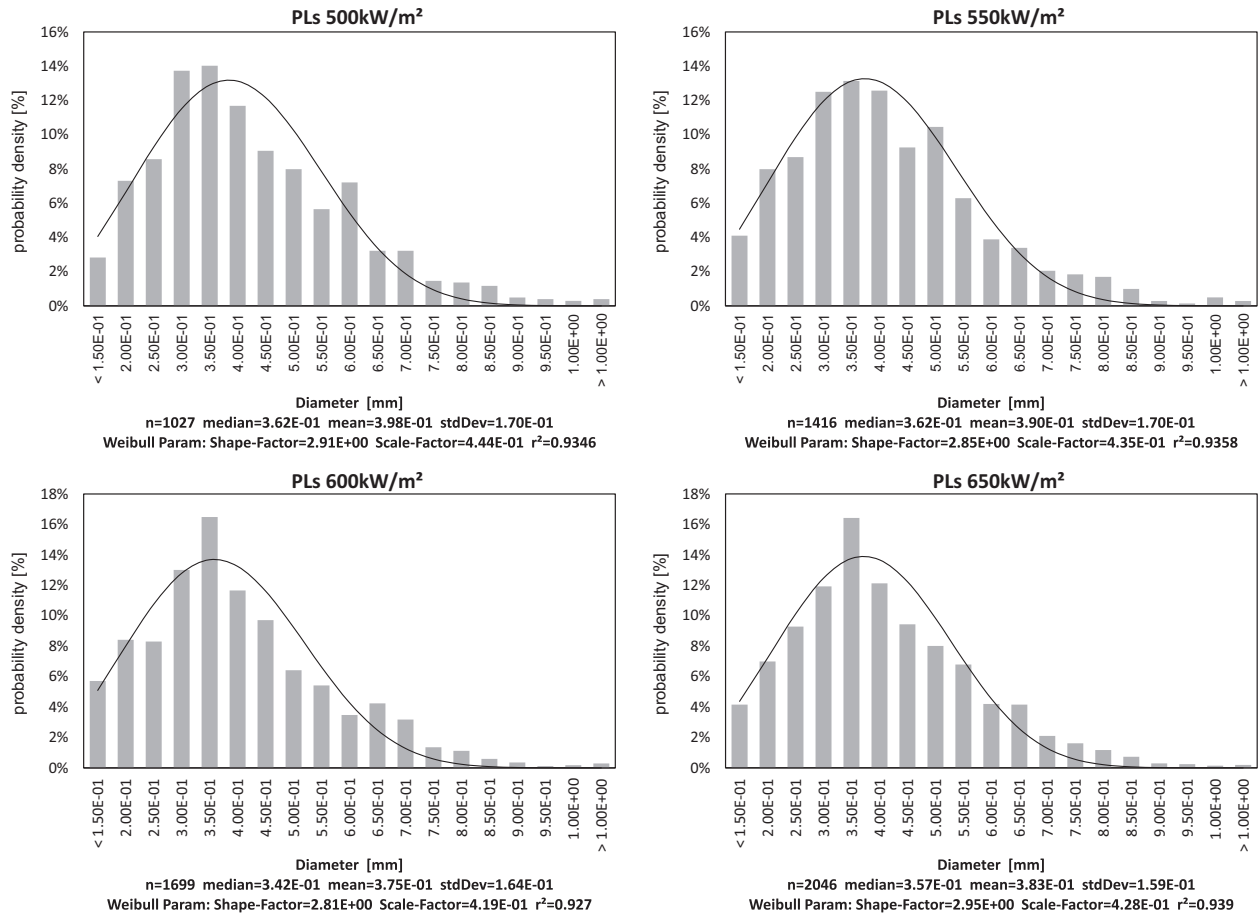


Fig. 13. PLs – Weibull diameter distribution, code test 8.

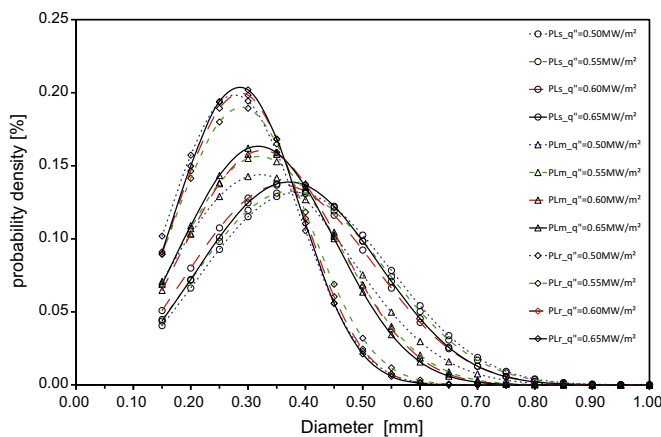


Fig. 14. Effect of surface roughness on the bubble size distribution, test code No. 8.

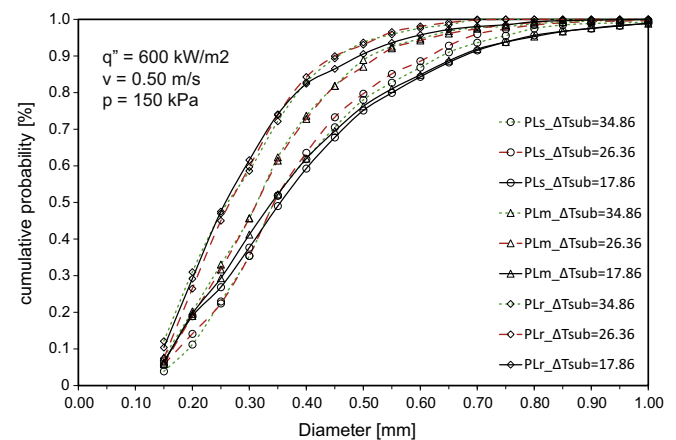


Fig. 15. Effect of subcooling on the bubble size distribution, test codes No. 1–8–15.

that increases the condensation rate in the case of higher subcooling, thus impeding the growth of the bubbles.

3.5. Effect of liquid velocity

The effect of liquid velocity was evaluated through tests 6, 8 and 10 (Fig. 16). The fluid velocity may have an influence on the bubble's diameter, but this influence is not as strong as that of other parameters studied. Maurus [44] indicated that an increase of liquid velocity denoted the presence of a larger percentage of smaller

bubbles, which was not totally confirmed by our experiments. It can be observed that the highest bulk temperature (0.9 m/s) led to smaller bubbles at each surface, but the intermediate and lower velocities did not confirm the existence of a direct relationship. Other researchers have found the same tendency [12,40,43].

3.6. Effect of heat flux

The effect of heat flux on diameter was not reflected in the same manner on each surface (Fig. 17), and it is difficult to establish

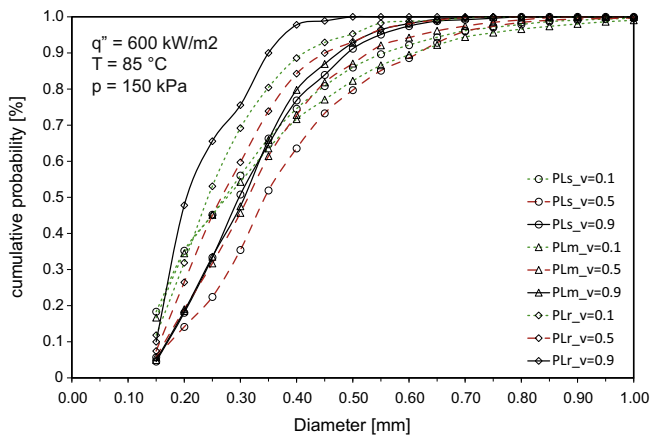


Fig. 16. Effect of liquid velocity on the bubble size distribution, test codes No. 6–8–10.

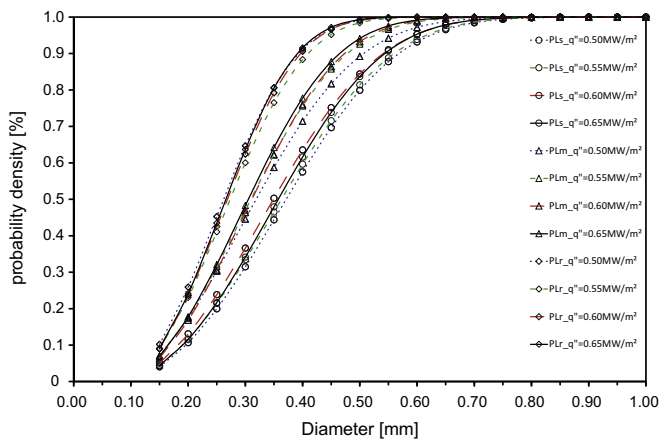


Fig. 17. Heat flux effect on the bubble size distribution, test code No. 8.

based on the experimental results obtained. It seems that higher heat fluxes tend towards bigger bubbles, which is consistent with the experimental investigations of Maurus [46] and Zhang [31]. However, other observations have been reported, for example, Tolubinsky and Kostanchuk [11] and Prodanovic [43] determined that the influence of heat flux could be neglected, whereas Abdelmessih et al. observed larger bubbles with an increase in heat flux [12].

As heat flux is varied during the test by changing the wall temperature and depending on surface morphology, it has been observed that wall overheat varies and consequently that the isolated effect of heat flux or wall temperature seems difficult to

isolate from the remaining factors. On one hand, an increase of surface temperature will develop a bigger thermal boundary layer, allowing bubbles to grow further. On the other hand, neighbouring cavities can become active in obstructing the proper development of the bubble, hence leading to a higher population of small and middle-sized bubbles. Finally, the increased population of bubbles may lead to their coalescence, which also may contribute to a general increase of size and a reduction in number density. However, it has to be kept in mind that when two identical bubbles merge, the resulting bubble has only a 26% larger diameter.

4. Discussion

Most of the experimental data shown in the previous sections agree with the experimental evidence reported in the literature, at least in the case of PLs, which is probably the surface morphologically closest to those generally employed by other authors. In terms of factors affecting bubble diameter, it can be summarized that bubbles are normally larger at lower pressures, lower levels of subcooling, and lower liquid velocity. The effect of heat flux was not clearly stated, which is also in agreement with previous works [11,12,43]. Therefore, the novelty of the experimental data shown is probably that the surface morphology has been characterised at a microscopic level and that the three surfaces tested proved that their morphologies were able to override the influence of many of the aforementioned parameters. The purpose of this section is to gather all the information shown and to propose a possible explanation.

Fig. 18 shows a virtual representation of the morphology of PLs, PLm and PLr with their typical bubble attached at a random spot. The presence of the bubble is important as this helps keep a sense of scale in the three axes. As shown in Fig. 18-a, it seems reasonable to believe that the micro-roughness present in the surface may serve as active sites but that once the bubble is nucleated, the morphology of the surface likely does not affect the size of the bubble. Hence, we consider that PLs is perfectly smooth in terms of bubble size and hence that the size distribution found for this surface will be similar to any smooth surface with the same thermal properties.

Fig. 18-b shows that although the surface of PLm is quite smooth, there are cavities that resulted from the EDM that were not erased by the ulterior sanding. Regarding flow structure, one can assume that the type of morphology generated will probably not affect the flow, hence in terms of fluid-dynamics, the bubble will develop in roughly the same environment as a smooth surface. An evidence of this behaviour can be inferred analysing the convective film coefficient that is almost the same for PLs and PLm (Fig. 19). This could be explained by the morphology of PLm shown in Fig. 3, which is generally smooth, showing a flat surface altered by only deep holes remained from the original EDM process. On the other hand, PLr results clearly rough in comparison with the other

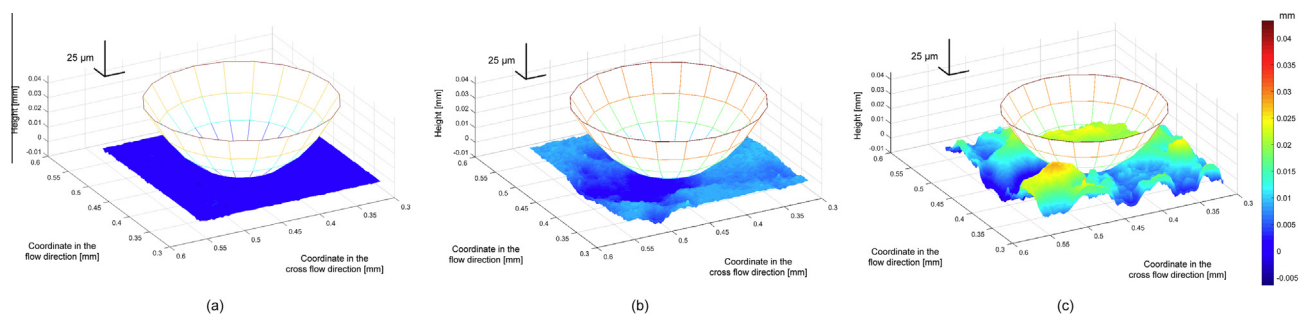


Fig. 18. Virtual representation of the typical diameter: (a) PLs, (b) PLm, (c) PLr.

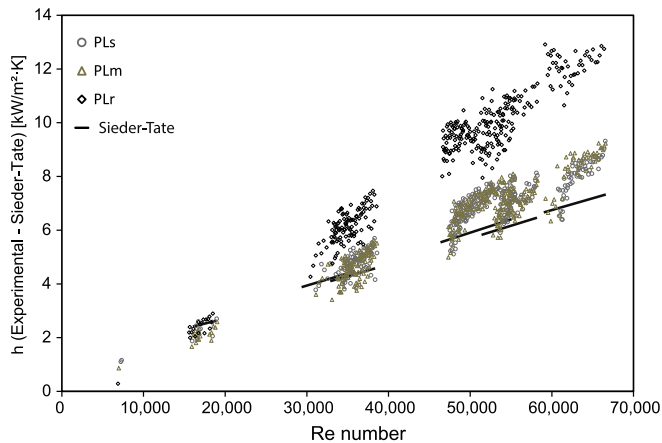


Fig. 19. Convective film coefficients vs. Re of the tested points for the three test parts.

two. The well-known Sieder and Tate correlation has been added to the chart for comparison purposes. Disagreements with experimental data for the smoothest surfaces mainly at high Re number could be the disturbance caused by any unavoidable misalignment of the test part and its PTFE skin with the rest of the channel. Also an incomplete development for the thermal boundary layer and the non-circular cross section of the channel could have influence.

Thus, regarding PLm, it is believed that the difference found in bubble population and size with respect to PLs must derive from other effects rather than the surrounding flow. One plausible explanation is that the deep cavities randomly spread over the surface serve as nucleation sites and therefore that their presence and activation in the vicinity of a developing bubble will obstruct their complete development. The surface itself cannot impose any morphological limit on the growth of particles, and consequently the largest bubbles observed in PLm are almost as large as those of PLs (see Fig. 14). However, as this surface has the capability to easily deploy new bubbles, its boiling pattern is composed of more but smaller bubbles than PLs. In fact, mechanistic models based on the balance of forces acting on a single bubble have suggested that the vertical balance of the forces may break when the bubble slows down or stops its growing [39], [41]. Hence, we can assume that the need to share overheating of the surface between neighbour nucleation sites may explain why PLm has a tendency to smaller bubbles than PLs and therefore that this morphology, although 'smooth' in terms of the flow, is somehow 'rough' in terms of nucleation.

Finally, PLr (Fig. 18-c) shows that its morphological features can easily affect the development of the bubbles and disturb the temperature and flow profile of the liquid at the bubble scale. This was experimentally confirmed by the increase of convective heat transfer observed (Fig. 19). The smaller typical bubble size, the higher number of bubbles below 150 μm , and the absence of large bubbles in their size distribution may be justified by the physical limit imposed by the peaks surrounding any viable nucleation site. However, other phenomena possibly contribute to a general reduction in a bubble's departure size, such as the perturbation of the flow that likely increases the dissipation of heat from the upper half of the bubble, neighbour bubbles being developed, and the instability of the liquid microlayer under the bubble due to the morphology of the surface.

Finally the fact that PLm and PLr did not show much influence from the subcooling in their size distribution (Fig. 15) may confirm that their size is less influenced by the surrounding flow than the morphology of the heating surface.

5. Conclusions

The influence of operational parameters on bubble population and size distribution has been experimentally studied in this work. To investigate the influence of surface conditions, three different copper heating elements have been used, which were manufactured to produce different superficial morphologies, and have been characterized. Two main aspects of the bubbles have been studied: number and size. Each of these aspects has been captured by means of an image processing tool, which has been developed for that purpose. The size of the bubbles has been arranged in several families and fitted to a Weibull distribution. The effect of system pressure, subcooling, liquid velocity, and heat flux were investigated.

It has been observed that liquid velocity has a very strong influence on bubble size and that heat flux showed only a slight tendency to increase bubble size. Subcooling affected the size of the bubbles departing from the smooth surface but had no apparent influence on the rougher ones.

Regarding surface morphology, rougher surfaces seem to generate smaller bubbles, which has been attributed to the sum of several factors. The vicinity of active sites and the presence of abrupt peaks that may impede the complete development of the bubbles seem to control the size of bubbles emerging from the EDM surface. The surface made by EDM and sanded afterwards (PLm) behaves as if it were smooth in terms of the flow but as if it were rough in terms of nucleation; the smoother surface (PLs) allowed the development of larger bubbles, probably as any similar smooth copper surface would have done.

Conflict of interest

None declared.

Appendix A. Supplementary data

Supplementary data associated with this article can be found, in the online version, at <http://dx.doi.org/10.1016/j.ijheatmasstransfer.2015.06.003>.

References

- [1] V. Dhir, Mechanistic prediction of nucleate boiling heat transfer – achievable or a hopeless task?, *J Heat Transfer* 128 (2006) 1–12.
- [2] J. Kim, Review of nucleate pool boiling bubble heat transfer mechanisms, *Int. J. Multiph. Flow* 35 (12) (2009) 1067–1076.
- [3] J.R. Thome, L. Cheng, G. Ribatski, L.F. Vales, Flow boiling of ammonia and hydrocarbons: a state-of-the-art review, *Int. J. Refrig.* 31 (4) (2008) 603–620.
- [4] D. Gorenflo, E. Baumhögger, G. Herres, S. Kotthoff, Prediction methods for pool boiling heat transfer: a state-of-the-art review, *Int. J. Refrig.* 43 (2014) 203–226.
- [5] C. Konishi, I. Mudawar, Review of flow boiling and critical heat flux in microgravity, *Int. J. Heat Mass Transfer* 80 (2015) 469–493.
- [6] M. Mpholo, T. Mathaba, H.H. Bau, A 2D analysis of surface roughness for prediction of boiling incipience, *Int. J. Heat Mass Transfer* 53 (7) (2010) 1313–1318.
- [7] S.C.P. Cheung, S. Vahaji, G.H. Yeoh, J.Y. Tu, Modeling subcooled flow boiling in vertical channels at low pressures. Part 1: assessment of empirical correlations, *Int. J. Heat Mass Transfer* 75 (2014) 736–753.
- [8] H. Zhang, I. Mudawar, M.M. Hasan, Assessment of dimensionless CHF correlations for subcooled flow boiling in microgravity and Earth gravity, *Int. J. Heat Mass Transfer* 50 (2007) 4568–4580.
- [9] R.L. Judd, K.S. Hwang, A comprehensive model for nucleate boiling heat transfer including microlayer evaporation, *Heat Transfer* 98 (1976).
- [10] F.C. Gunther, Photographic study of surface-boiling heat transfer to water with forced convection, *Trans. ASME J.* 73 (1951) 115–123.
- [11] V.I. Tolubinsky, D.M. Kostanchuk, Vapour bubbles growth rate and heat transfer intensity at subcooled water boiling, *Proceedings of the 4th International Heat Transfer Conference*, vol. 5 (1970) paper no. B-2.8.
- [12] A.H. Abdelmessih, F.C. Hooper, S. Nangia, Flow effects on bubble growth and collapse in surface boiling, *Int. J. Heat Mass Transfer* 15 (1972) 115–125.

- [13] E.L. Bibeau, M. Salcudean, A study of bubble ebullition in forced-convective subcooled nucleate boiling at low pressure, *Int. J. Heat Mass Transfer* 37 (1994) 2245–2259.
- [14] O. Zeitoun, M. Shoukri, "Bubble behavior and mean diameter in subcooled flow boiling" *Trans. ASME, J. Heat Transfer* 118 (1996) 110–116.
- [15] M. Jakob, Heat transfer in evaporation and condensation-I, *Mech. Eng. (Am. Soc. Mech. Eng.)* 58 (1936) 643–660.
- [16] W.M. Rohsenow, A method of correlating heat-transfer data for surface boiling of liquids, *Trans. ASME* 74 (1952) 969–976.
- [17] C. Corty, A.S. Foust, Surface variables in nucleate boiling, *Chem. Eng. Prog. Symp. Ser.* 21 (17) (1955) 1.
- [18] R.I. Vachon, G.H. Nix, G.E. Tanger, R.O. Cobb, Pool boiling heat transfer from Teflon-coated stainless steel, *ASME J. Heat Transfer* 91 (1969) 364–370.
- [19] S.G. Bankoff, Entrapment of gas in the spreading of liquid over a rough surface, *AIChE J.* 4 (1) (1958) 24–26.
- [20] J.D. Wallis, P. Griffith, The role of surface conditions in nucleate boiling" *Chemical Engineering Progress Symposium Series*, AIChE 30 (56) (1960) 49–63.
- [21] P. Berenson, Experiments on pool-boiling heat transfer, *Int. J. Heat Mass Transfer* 5 (10) (1962) 985–999.
- [22] A.E. Bergles, W.M. Rohsenow, The determination of forced-convection surface-boiling heat transfer, *J. Heat Transfer* 1 (1964) 365–372.
- [23] B.B. Mikic, W.M. Rohsenow, A new correlation of pool boiling data, including the effect of heating surface characteristics, *ASME J. Heat Transfer* 9 (1969) 245–250.
- [24] Y. Hsu, On the size range of active nucleation cavities on a heating surface, *J. Heat Transfer* 84 (3) (1962) 207–213.
- [25] I. Pioro, W. Rohsenow, S. Doerffer, Nucleate pool-boiling heat transfer. I: review of parametric effects of boiling surface, *Int. J. Heat Mass Transfer* 47 (23) (2004) 5033–5044.
- [26] J.M.S. Jabardo, An overview of surface roughness effects on nucleate boiling heat transfer, *Open Transp. Phenom. J.* 2 (2010) 24–34.
- [27] B.J. Jones, J.P. McHale, S.V. Garimella, The influence of surface roughness on nucleate pool boiling heat transfer, *J. Heat Transfer* 131 (2009).
- [28] J.P. McHale, S.V. Garimella, Nucleate boiling from smooth and rough surfaces. – Part 2: analysis of surface roughness effects on nucleate boiling, *Exp. Thermal Fluid Sci.* 44 (2013) 439–455.
- [29] B.J. Zhang, K.J. Kim, Nucleate pool boiling heat transfer augmentation on hydrophobic self-assembly mono-layered alumina nano-porous surfaces, *Int. J. Heat Mass Transfer* 73 (2014) 551–561.
- [30] C.Y. Lee, B.J. Zhang, K.J. Kim, Morphological change of plain and nano-porous surfaces during boiling and its effect on nucleate pool boiling heat transfer, *Exp. Thermal Fluid Sci.* 40 (2012) 150–158.
- [31] B.J. Zhang, K.J. Kim, H. Yoon, Enhanced heat transfer performance of alumina sponge-like nano-porous structures through surface wettability control in nucleate pool boiling, *Int. J. Heat Mass Transfer* 55 (25) (2012) 7487–7498.
- [32] C.H. Wang, V.K. Dhir, On the gas entrapment and nucleation site density during pool boiling of saturated water, *ASME J. Heat Transfer* 115 (1993) 670–679.
- [33] V.K. Dhir, G.R. Warrier, E. Aktinol, Numerical simulation of pool boiling: a review, *J. Heat Transfer* 135 (6) (2013).
- [34] M. Matkovic, B. Koncar, Bubble departure diameter prediction uncertainty, *Sci. Technol. Nucl. Instal.* 2012 (2012).
- [35] A. Mukherjee, S.G. Kandlikar, Numerical study of single bubbles with dynamic contact angle during nucleate pool boiling, *Int. J. Heat Mass Transfer* 50 (2007) 127–138.
- [36] L. Zou, B.G. Jones, Heating surface material's effect on subcooled flow boiling heat transfer of R134a, *Int. J. Heat Mass Transfer* 58 (1) (2013) 168–174.
- [37] A.P. Hattton, I.S. Hall, Photographic study of boiling on prepared surfaces, *Proceedings of the Third International Heat Transfer Conference*, vol. 4 (1966) 24–37.
- [38] H.C. Unal, Maximum bubble diameter, maximum bubble-growth time and bubble-growth rate during the subcooled nucleate flow boiling of water up to 17.7 MN/m², *Int. J. Heat Mass Transfer* 19 (6) (1976) 643–649.
- [39] J.F. Klausner, R. Mei, D.M. Bernhard, L.Z. Zeng, Vapor bubble departure in forced convection boiling, *Int. J. Heat Mass Transfer* 36 (3) (1993) 651–662.
- [40] S.G. Kandlikar, B.J. Stumm, Control volume approach for investigating forces on a departing bubble under subcooled flow boiling, *J. Heat Transfer* 117 (4) (1995) 990–997.
- [41] M. Colombo, M. Fairweather, Prediction of bubble departure in forced convective boiling: a mechanistic model, *Intern* 85 (2015) 135–146.
- [42] M.C. Paz, M. Conde, E. Suárez, M. Concheiro, On the effect of surface roughness and material on the subcooled flow boiling of water: experimental study and global correlation, *Exp. Thermal Fluid Sci.* 64 (2015) 114–124.
- [43] V. Prodanovic, D. Fraser, M. Salcudean, Bubble behavior in subcooled flow boiling of water at low pressures and low flow rates, *Int. J. Multiph. Flow* 28 (1) (2002) 1–19.
- [44] R. Maurus, V. Ilchenko, T. Sattelmayer, Study of the bubble characteristics and the local void fraction in subcooled flow boiling using digital imaging and analysing techniques, *Exp. Thermal Fluid Sci.* 26 (2) (2002) 147–155.
- [45] L.-H. Chien, R.L. Webb, Measurement of bubble dynamics on an enhanced boiling surface, *Exp. Thermal Fluid Sci.* 16 (3) (1998) 177–186.
- [46] R. Maurus, T. Sattelmayer, Bubble and boundary layer behaviour in subcooled flow boiling, *Int. J. Therm. Sci.* 45 (3) (2006) 257–268.